Research article

NMR IN BIOMEDICINE

Received: 05 December 2012, Revised: 17 April 2013, Accepted: 17 May 2013, Published online in Wiley Online Library: 18 June 2013

(wileyonlinelibrary.com) DOI: 10.1002/nbm.2989

Resonant inductive decoupling (RID) for transceiver arrays to compensate for both reactive and resistive components of the mutual impedance

Nikolai I. Avdievich*, Jullie W. Pan and Hoby P. Hetherington

Transceiver surface coil arrays improve transmit performance ($B_1/\sqrt{kW}$) and B_1 homogeneity for head imaging up to 9.4 T. To further improve reception performance and parallel imaging, the number of array elements must be increased with a corresponding decrease in their size. With a large number of small interacting antennas, decoupling is one of the most challenging aspects in the design and construction of transceiver arrays. Previously described decoupling techniques using geometric overlap, inductive or capacitive decoupling have focused on the elimination of the reactance of the mutual impedance only, which can limit the obtainable decoupling to –10 dB as a result of residual mutual resistance. A novel resonant inductive decoupling (RID) method, which allows compensation for both reactive and resistive components of the mutual impedance between the adjacent surface coils, has been developed and verified experimentally. This method provides an easy way to adjust the decoupling remotely by changing the resonance frequency of the RID circuit through the adjustment of a variable capacitor. As an example, a single-row (1×16) 7-T transceiver head array of $n = 16$ small overlapped surface coils using RID decoupling between adjacent coils was built. In combination with overlapped coils, the RID technique achieved better than –24 dB of decoupling for all adjacent coils. Copyright © 2013 John Wiley & Sons, Ltd.

Keywords: RF head coil; transceiver arrays; array decoupling; high-field MRI; mutual resistance

INTRODUCTION

At high magnetic field strengths, where the object size becomes comparable to the radiofrequency (RF) wavelength (e.g. body imaging at 3 T and above, head imaging at 7 T and above), increased RF inhomogeneity, decreased transmit efficiency ($\mu T/\sqrt{W}$) and increasing local specific absorption rate (SAR) pose significant limitations for conventional single-channel transmit volume coils. To overcome these limitations, substantial effort has been focused on the development of transceiver phased arrays consisting of multiple independent (i.e. decoupled) RF antennas used simultaneously for both transmission and reception. Transceiver arrays provide improved homogeneity, enhanced transmit efficiency and decreased SAR through the use of RF shimming (1–5) and parallel transmission (6–8). Head arrays with surface coils as individual elements have been successfully utilized at 7 T (4,9,10) and above (11). In the surface coil array, loops of the RF current are normally positioned parallel to the surface of the array holder which circumscribes the head, as opposed to stripline designs (1,12,13) in which the current flows in a plane perpendicular to the surface of the head. This orientation of antennas minimizes the mutual inductive coupling between the array's elements and simplifies decoupling by largely limiting significant coupling to only adjacent elements (14). As transceiver arrays can also be used as conventional phased arrays for reception, receive sensitivity can, in principle, also be maintained. However, to provide sufficient coverage of the entire object during transmission and a high signal-to-noise ratio (SNR) comparable with multi-channel receive-only arrays, transceiver arrays should consist of smaller overlapped RF surface coils. With a large number of interacting RF antennas, decoupling is one of the most challenging and critical aspects in the design and construction of transceiver arrays. The fact that the same array elements are used for both transmission and reception dictates that preamplifier decoupling (15) cannot be utilized.

Overlapping of adjacent surface coils is one of the most common inductive decoupling techniques (15–17), and enables larger and greater numbers of RF coils to be used for a given circumference of the array. Maintaining the size of the individual coils in the array is important to preserve the penetration depth for RF transmission. Adjacent overlapped surface coils under loading can generate substantial mutual resistance R_{12} (15,18), and often cannot be decoupled using additional common capacitive (1,10,12,19) or inductive (4,9,11,15) decoupling methods, which compensate only for the mutual reactance. The mutual resistance is produced as a result of common current paths between the coil pair within the sample. For example, for a pair of overlapped loaded surface coils, the R_{12}/R ratio, where R

* *Correspondence to: N. I. Avdievich, Department of Neurosurgery, Yale University, MRRC/TAC, 300 Cedar St., New Haven, CT 06520, USA.*
E-mail: nikolai.avdievich@gmail.com

N. I. Avdievich, J. W. Pan, H. P. Hetherington
Department of Neurosurgery, Yale University, New Haven, CT, USA

Abbreviations used: *RID, resonant inductive decoupling; RF, radiofrequency; SAR, specific absorption rate; SNR, signal-to-noise ratio.*

Copyright © 2013 John Wiley & Sons, Ltd.

is the resistance of each surface coil, can measure from 0.2 to 0.4 (15,18). This corresponds to a residual coupling in the range −14 to −8 dB.

Resonant inductive decoupling (RID) provides a way to compensate for both the reactive and resistive components of the mutual impedance Z_{12} (20). It also offers an easy way to adjust the decoupling, by changing the resonance frequency of the decoupling circuit through the adjustment of a single variable capacitor. However, the placement and geometry of these RID elements are critical, as the RF field generated by RID can significantly alter the RF field of the array.

In this work, we describe a novel RID technique, which provides for the decoupling of array elements, as well as the minimization of resistive coupling. We also demonstrate the importance of both the geometry and orientation of the resonant loops in the RID element with respect to each other and the array itself in optimizing the decoupling performance. As a demonstration of the technique, we built a densely populated single-row (1 × 16) transceiver head array of small overlapped surface coils and acquired images of the human head at 7 T.

THEORY

In this work, we developed a new technique, which improves the decoupling of individual antennas in a transceiver array. The term 'decoupling' is used to describe the process of eliminating a 'crosstalk' or energy transfer between two coupled antennas through the shared impedance Z_{12}. The efficiency of decoupling as applied to transmission is evaluated by measuring the transmission parameter S_{12}, which is directly related to the Z_{12} value. In this sense, the resistive and reactive components of Z_{12} simply describe the amplitude and phase relationship of a signal propagating between ports of two coupled antennas. As applied to reception, the mutual resistance measured between two coupled antennas is often related to their noise correlation (15,18). Evaluation of the noise correlation between two resonant coils additionally coupled to a third resonant decoupling circuit is more complicated than that just for a pair of coils. It requires thorough theoretical consideration and is beyond the scope of this work.

Figure 1 shows two resonant decoupling circuits inductively coupled to a pair of surface coils. In the presence of a sample, the mutual impedance Z_{12} may contain a substantial resistive component R_{12} as a result of common current paths between the coil pair within the sample. Figure 1A presents a 'butterfly' ('figure-eight') RID coil, whereas Fig. 1B depicts a regular surface coil. The matrix for the Kirchhoff equations describing the 'figure-eight' RID coil is given by:

$$\begin{pmatrix} V_1 \\ 0 \\ V_2 \end{pmatrix} = \begin{pmatrix} Z_1 & j\omega_L M_0 & -j\omega_L M + R_{12} \\ j\omega_L M_0 & Z_0 & -j\omega_L M_0 \\ -j\omega_L M + R_{12} & -j\omega_L M_0 & Z_2 \end{pmatrix} \begin{pmatrix} I_1 \\ I_0 \\ I_2 \end{pmatrix} \quad [1]$$

where Z_0, Z_1 and Z_2 are the corresponding impedances of the RID circuit and the two surface coils, M_0 is the mutual inductance between the RID and each surface coil (for simplicity, we assumed them to be equal) and ω_L is the resonance frequency of the surface coils. Solving for V_1 and V_2, we obtain:

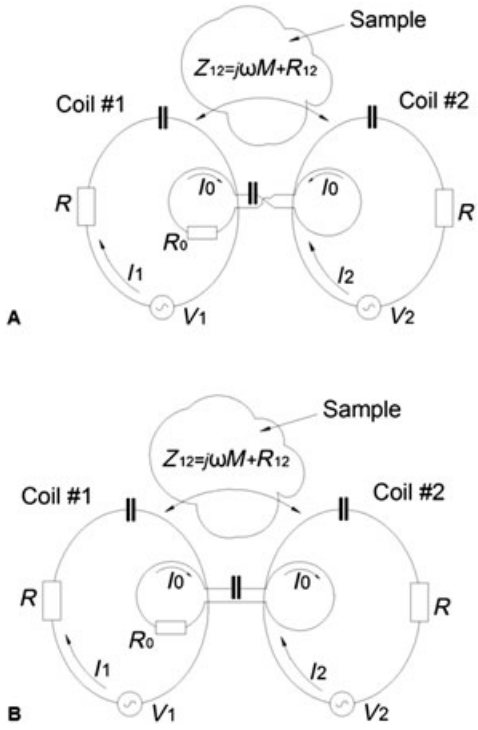

Figure 1. Schematic diagrams demonstrating the general concept of the construction of resonant inductive decoupling (RID) circuits using a 'butterfly' ('figure-eight') coil (A) and a regular surface coil (B). Two geometrically identical resonant coils #1 and #2 are coupled with their shared impedance Z_{12} and characterized by the inductance L and the resistance R. In the presence of the sample, the mutual impedance Z_{12} contains both reactive ($j\omega M$) and resistive (R_{12}) components. The RID circuits shown in (A) and (B) are characterized by the inductance L_0 and the resistance R_0.

$$\begin{pmatrix} V_1 \\ V_2 \end{pmatrix} = \begin{pmatrix} Z_1 + \frac{\omega_L{}^2 M_0^2}{Z_0} & -j\omega_L M + R_{12} - \frac{\omega_L{}^2 M_0^2}{Z_0} \\ -j\omega_L M + R_{12} - \frac{\omega_L{}^2 M_0^2}{Z_0} & Z_2 + \frac{\omega_L{}^2 M_0^2}{Z_0} \end{pmatrix} \begin{pmatrix} I_1 \\ I_2 \end{pmatrix} \quad [2]$$

Similarly, for the RID design shown in Fig. 1B, we obtain:

$$\begin{pmatrix} V_1 \\ V_2 \end{pmatrix} = \begin{pmatrix} Z_1 + \frac{\omega_L{}^2 M_0^2}{Z_0} & -j\omega_L M + R_{12} + \frac{\omega_L{}^2 M_0^2}{Z_0} \\ -j\omega_L M + R_{12} + \frac{\omega_L{}^2 M_0^2}{Z_0} & Z_2 + \frac{\omega_L{}^2 M_0^2}{Z_0} \end{pmatrix} \begin{pmatrix} I_1 \\ I_2 \end{pmatrix} \quad [3]$$

Near the resonance, Z_0 can be approximated as $Z_0 \approx 2jL_0(\omega_L - \omega_0) + R_0 = 2jL_0\Delta\omega + R_0$, where ω_0 is the resonance frequency of the decoupling circuit, and L_0 and R_0 are its inductance and resistance. For the off-diagonal elements in Equation [2], we obtain:

$$-j\omega_L M + R_{12} - \frac{\omega_L{}^2 M_0^2}{Z_0} \approx -j\omega_L L\left(k - \frac{k_0^2}{2\xi}\right) + R_{12} - \frac{R}{4}\frac{k_0^2}{\xi^2}\frac{Q}{Q_0} \quad [4]$$

where $\xi = \Delta\omega/\omega_L$, R and L are the resistance and inductance of the surface coils, and Q_0 and Q are the corresponding Q factors of the

Copyright © 2013 John Wiley & Sons, Ltd.

RID and surface coils. We have also taken into account that $M_0 = k_0(LL_0)^{1/2}$ and $M = kL$, where k and k_0 are the corresponding coupling coefficients. Again, for simplicity, we assume that R, L and Q are the same for both surface coils. From Equation [4] when $\Delta\omega > 0$ ($\omega_0 < \omega_L$), both the real and imaginary components of Z_{12} can be cancelled. To cancel the mutual reactance:

$$k_0^2 = 2k\xi \qquad [5]$$

Both the reactive and resistive components of Z_{12} are cancelled when:

$$k_0 = k\sqrt{\frac{Q_0}{\eta Q}} \text{ and } \xi = \frac{k}{2\eta}\frac{Q}{Q_0} \qquad [6]$$

where η is the R_{12}/R ratio. Thus, by varying the coupling coefficient k_0 and the frequency shift ξ, both the real and imaginary components of Z_{12} can be cancelled. Similarly, for the RID coil shown in Fig. 1B [Equation [3]], the off-diagonal elements are given by $-j\omega_L L\left(k + \frac{k_0^2}{2\xi}\right) + R_{12} + \frac{R}{4}\frac{k_0^2}{\xi^2}\frac{Q}{Q_0}$. Therefore, the reactive component of Z_{12} can be cancelled when $\Delta\omega < 0$ ($\omega_0 > \omega_L$). However, this RID coil only adds to R_{12} as both resistive components have the same sign. The mutual inductance is eliminated when $k_0^2 = -2k\xi$. Thus, this circuit can also be used to compensate for the mutual reactance between two surface coils when $\xi < 0$ ($\omega_0 > \omega_L$). However, ξ should be sufficiently large so as not to increase the resistive coupling. This can be achieved if the RID coil has a larger coupling coefficient k_0 (e.g. larger loops). A major difference between the two decoupling circuits shown in Figs 1A and 1B is that magnetic fluxes generated by surface coils #1 and #2 produce voltages of opposite sign in the 'figure-eight' RID coil (Fig. 1A) *versus* voltages of the same sign in the RID circuit shown in Fig. 1B. A situation similar to that shown in Fig. 1A can be realized in several different ways, as shown, for example, in Fig. 2A–D. The decoupling circuits shown in Fig. 2A (21) and Fig. 2B (22) have been described previously. For all of these cases, the Kirchhoff equations in Equation [2] apply, such that these RID coils can decouple a pair of array elements when $\xi > 0$ ($\omega_0 < \omega_L$), as well as compensate for the resistive components of Z_{12}. Figures 2E and 2F present two additional examples of RID circuits similar to that shown in Fig. 1B and described by Equation [3]. Again, these RID circuits cancel the mutual inductive coupling when $\xi < 0$ ($\omega_0 > \omega_L$), but cannot compensate for the resistive component of Z_{12}. A design similar to that shown in Fig. 2F has also been described previously (23).

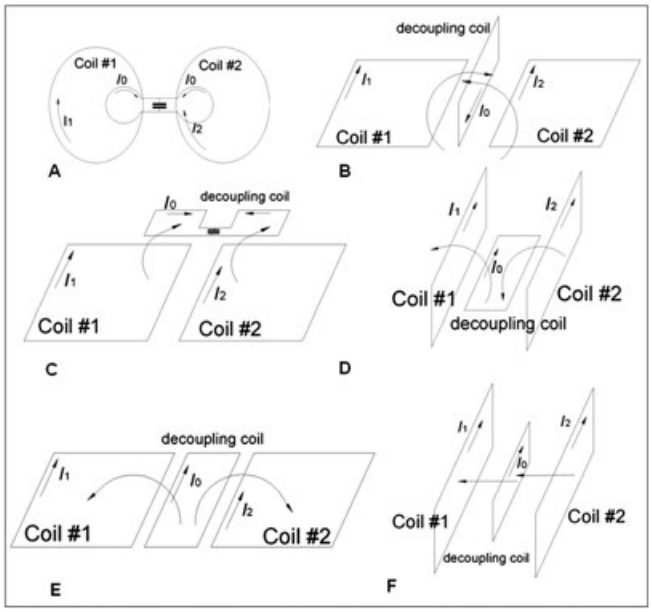

Figure 2. Schematic diagrams of various resonant inductive decoupling (RID) circuits.

It is also of importance to evaluate the current I_0 flowing in the RID circuit. For example, for the 'figure-eight' RID, from Equations [1] and [5], we obtain:

$$I_0 = \frac{j\omega_L M_0}{Z_0}(I_2 - I_1) \approx \frac{k_0}{2\xi}\sqrt{\frac{L}{L_0}}(I_2 - I_1) = \frac{k}{k_0}\sqrt{\frac{L}{L_0}}(I_2 - I_1) \qquad [7]$$

EXPERIMENTAL DETAILS

To demonstrate these concepts, we built several 298-MHz (^{1}H frequency at 7 T) two-coil arrays with resonant (RID) and conventional non-RID circuits for comparison. All of these arrays were built using nonoverlapped rectangular surface coils of the same size (width, 7.5 cm; length, 9 cm) with a 13-mm gap between adjacent ($\Delta n = 1$) coils. Each surface coil was formed from copper tape (width, 6.4 mm) with six capacitors (100C series, American Technical Ceramics, Huntington Station, NY, USA) uniformly distributed along the coil's length. All the coils were individually tuned and matched using variable capacitors (Voltronics, Denville, NJ, USA). The RID coils (4 mm ID) were built using 18-gauge copper magnet wire (diameter, 1 mm) and positioned at ~10 mm distance from the surface coil plane to increase the separation from the sample.

We also built a 16-coil, single-row (1 × 16) array consisting of smaller (width, 5.6 cm; length, 9 cm) overlapped rectangular surface coils (Fig. 3). A schematic diagram of an individual surface coil is shown in Fig. 4. The surface coils were formed using 5-mm copper tape and overlapped by 12 mm. The coupling between adjacent coils ($\Delta n = 1$), both reactive and resistive, was compensated using RID circuits. RID circuits (3 mm ID) were constructed using 20-gauge (diameter, 0.8 mm) magnet wire. The proximity of the next-nearest surface coils (i.e. $\Delta n = 2$) resulted in mutual inductive coupling of ~5 nH ($k \sim 0.03$). This coupling was eliminated by the use of conventional non-RID transformer (4,9), as shown in Fig. 4. For the non-RID circuits, we used two-turn small (diameter, 2.3 mm) coils made of 20-gauge magnet wire and wound in opposite directions, instead of single-loop coils as described previously (4,9). To decrease radiation losses (24), a shield (50-μm polyamide film with a 5-μm copper layer; Sheldahl, Northfield, MN, USA) was placed 4 cm away from the surface coils. To make sure that the RF field produced by the RID circuits was well localized and did not perturb the B_1 of the array within the head, we measured transmit B_1 maps (phase and amplitude) (25). We then compared them with the maps obtained with the same arrays, but decoupled using conventional non-RID, which does not perturb significantly the RF field profile (4,9).

To mimic head loading conditions, we constructed two phantoms, both filled with NaCl and sucrose in water (26). The

Copyright © 2013 John Wiley & Sons, Ltd.

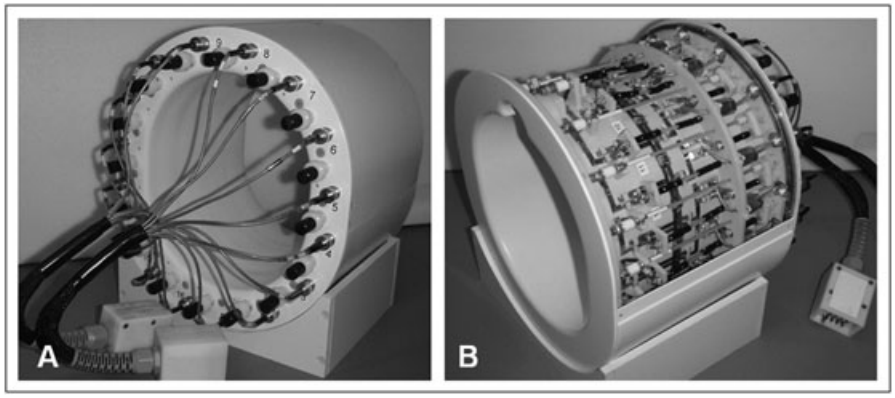

Figure 3. Photographs of the back (A) and front (B) sides of the 1 × 16 phased array. Photograph in (B) shown with the top cover removed.

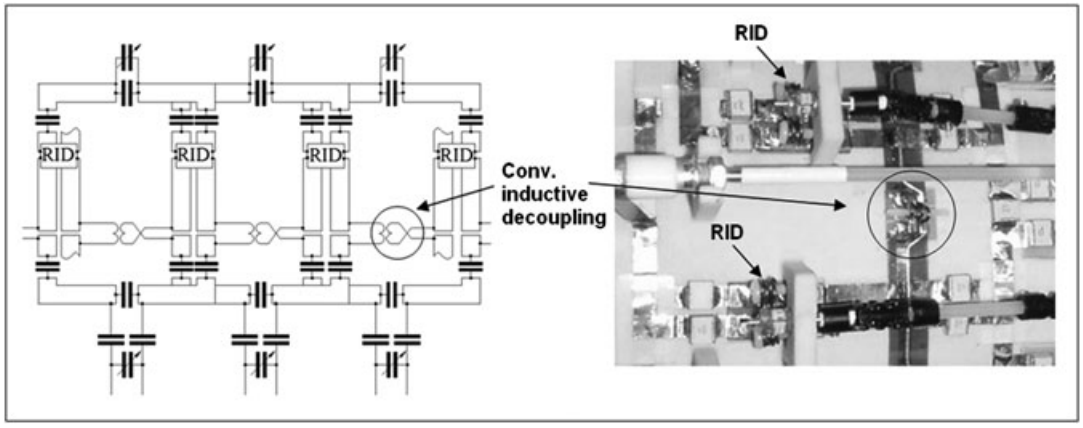

Figure 4. Schematic diagrams of the individual surface coils, including matching and decoupling networks.

percentage by weight measured 41.7%, 56.3% and 2.1% for water, sucrose and NaCl, respectively. The conductivity and dielectric permittivity measured 0.57 S/m and 52, respectively, which approximates that reported for the human head at 300 MHz (^{1}H resonance frequency at 7 T). The two-coil arrays were evaluated using a 2.0-L spherical phantom (diameter, 16 cm). The 1 × 16 array was evaluated using a cylindrical phantom with an elliptical cross-section (14 cm × 17 cm). With the described solution, this provides loading similar to that of an average-sized human head. Coupling coefficients k and k_0 were estimated as described previously (27). The Q factors of RID circuits were estimated from the frequency dependence of S_{12} and measured using a weakly coupled pair of pick up coils (28). The Q factors of the surface coils were evaluated using the frequency dependence of S_{11} (28). For the 1 × 16 array, Q_U of individual surface coil elements measured 270. Q_L measured on an average-sized human head varied from ~70 ($Q_U/Q_L = 3.9$) for the posterior coils (closest to the head) to ~100 ($Q_U/Q_L = 2.7$) for the anterior coils (furthest from the head).

All data were collected using a 7-T Agilent (Santa Clara, CA, USA) system. To test the coil performance, gradient echo images (256 × 256 × 13 slices) from an adult subject and a phantom were collected using slice thickness/gap = 2/8 mm, field of view of 19.2 cm × 19.2 cm, TR = 400 ms and nominal flip angle of 15°. B_1 maps of the individual coils (single coil transmitting) or the combined array (all coils transmitting simultaneously) were collected using a rapid gradient echo dual angle method (25) with 64 × 64 resolution, TR = 1 s and slice thickness/gap = 5/5 mm centered on the matched gradient echo images. All human studies were performed under an Institutional Review Board (Human Investigations Committee)-approved development project.

RESULTS

First, the geometry of the RID circuit was optimized to ensure that it did not perturb the profile of the RF magnetic field B_1 produced by a pair of well-decoupled surface coils. Initially, we evaluated the two RID geometries shown in Figs 2A (21) and 2B (22). We also evaluated the effect of positioning the 'figure-eight' decoupling coil perpendicular to the plane of the surface coils (Fig. 2D) to minimize distortion of the B_1 field. Table 1 summarizes the data for the five different configurations, including their size, the coupling coefficient k_0, the resonance frequency and the Q factor. Figure 5A–D shows axial maps of the amplitude of the combined simultaneous B_1^+ for five slices separated by 10 mm located near the surface coil center. The maps were obtained using two-coil arrays with conventional non-RID (Fig. 5A), three different sizes (Fig. 5B–D) of 'flat' RIDs (Fig. 2A) and an optimized RID (Fig. 5E) described below. In an attempt to minimize the distortion of the B_1 field by the 'flat' RID circuit, we started with a small coil of 16 mm in diameter (Fig. 5B). As shown in Table 1, the value of f_0 was only 5 MHz less than f_L

Copyright © 2013 John Wiley & Sons, Ltd.

Table 1. Parameters of resonant inductive decoupling (RID) circuits

RID	Loop size	k_0	f_0 (MHz)	ξ	Q_0
Figure 2A	Diameter, 16 mm	0.05	293	0.017	280
Figure 2A	Diameter, 22 mm	0.06	289	0.03	325
Figure 2A	Diameter, 28 mm	0.09	280	0.064	440
Figure 2B	15 mm × 60 mm	0.06	288	0.034	380
Figure 2C	20 mm× 20 mm	0.04	294	0.013	400

($\xi = 0.017$). Despite the small size of the RID coil, the B_1 profile of the array was altered significantly at the surface of the sample. To minimize the RF field distortions by increasing ξ, whilst keeping the same RID geometry, we increased the RID coil diameter to 22 mm and 28 mm, resulting in $\xi = 0.03$ ($f_0 = 289$ MHz) and $\xi = 0.06$ ($f_0 = 280$ MHz), respectively. However, this caused similar distortions in the B_1 field (Fig. 5C, D). All other types of RIDs presented in Table 1 also produced substantial B_1 field distortion.

To minimize the B_1 field distortion by localizing the RID RF field and, at the same time, keeping sufficiently large k_0 and ξ, we constructed optimized RID circuits (Fig. 6). The B_1 map (Fig. 5E) obtained using the two-coil array with the optimized RID demonstrates minimal distortion and is very similar to that obtained using the array with conventional non-RID. The optimized RID circuit consisted of two small two-turn inductors connected in series with the surface coils and an electrically insulated resonant coil with a pair of two-turn loops coupled to each surface coil (Fig. 6, Table 2). To match Equation [2] (i.e. the magnetic fluxes generated by adjacent surface coils produce voltages of opposite sign in the RID loops), all four two-turn loops of the RID circuit should be wound in appropriate directions, i.e. two of the four loops were wound clockwise and two counterclockwise (Fig. 6). In spite of the much smaller size of the optimized RID circuits, we obtained substantially larger k_0 values (Table 2) when compared with nonoptimized RIDs (Table 1).

Figure 7 shows the dependence of the loaded Q factor Q_L, measured for the two-coil array decoupled using conventional non-RID, optimized RID and the 16-mm 'flat' RID (Fig. 2A), on the distance between the phantom and the surface coils. As shown in Fig. 7, the presence of the nonoptimized small RID increases substantially Q_L at distances up to 7 cm, which is much greater than the size of the RID circuit itself.

For the 1 × 16 array using optimized RID (Fig. 6) in combination with overlapping, we obtained decoupling better than −24 dB for all adjacent coils. Decoupling of −19 dB or better was obtained for all other surface coils. Figure 8A shows axial B_1^+ maps for individual surface coil elements, demonstrating good decoupling. Figures 8B and 8C show the combined axial image and corresponding B_1^+ map obtained using the 16-coil (1 × 16) overlapped array. Homogeneity was evaluated as the standard deviation of B_1^+ over the entire slice, and measured 9.2%.

DISCUSSION

In the presence of lossy human tissue, the mutual impedance Z_{12} may include both reactive and resistive components. For

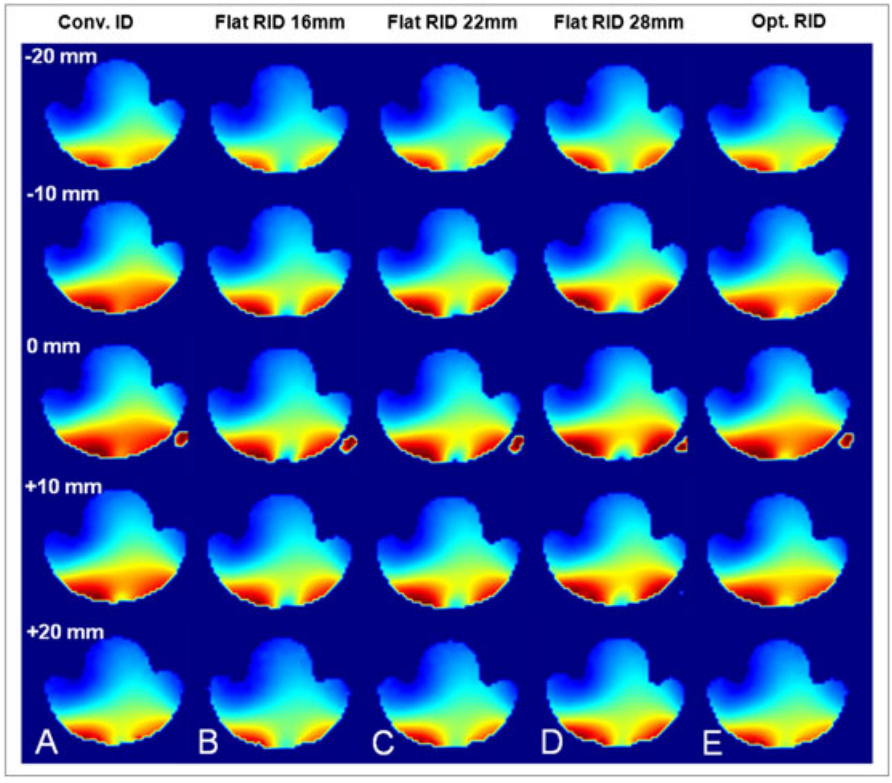

Figure 5. Axial maps of the amplitude of the combined simultaneous B_1^+ for five slices separated by 10 mm located near the surface coil center. The maps were obtained using two-coil arrays with conventional nonresonant inductive decoupling (A), three different sizes (B–D) of 'flat' resonant inductive decoupling (RID) circuits (Fig. 2A) and the optimized RID (E).

Copyright © 2013 John Wiley & Sons, Ltd.

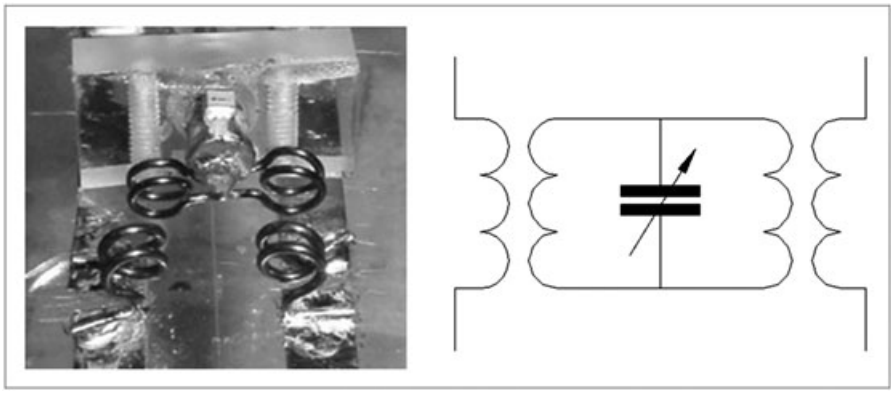

Figure 6. Photograph and schematic diagram of the optimized resonant inductive decoupling (RID) circuit.

Table 2. Parameters of the optimized resonant inductive decoupling (RID) circuit

k_0	Loop size	f_0 (MHz)	ξ	Q_0
0.14	Diameter, 4 mm	259	0.13	300

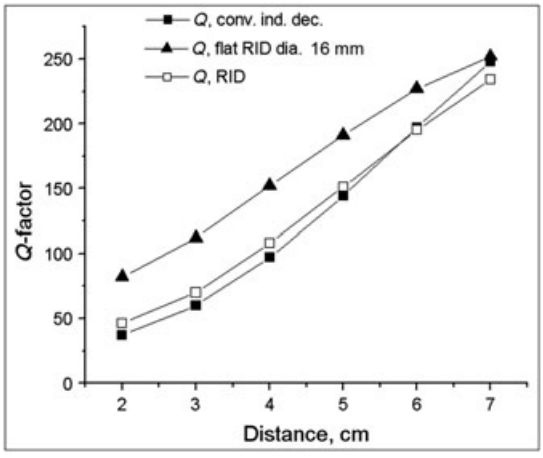

Figure 7. Dependence of the loaded Q factor Q_L, measured for the two-coil array decoupled using non-resonant inductive decoupling, optimized resonant inductive decoupling (RID) and the 16-mm 'flat' RID (Fig. 2A), on the distance between the phantom and the surface coils.

example, in the case of overlapping surface coils, which is one of the most common inductive decoupling techniques, the resistive component can reach substantial values (15,18). Conventional capacitive and inductive decoupling methods only compensate for the reactive component of Z_{12}, and thus do not provide sufficient decoupling of the elements within an array of overlapped coils. For example, for an overlapped 1×16 array when unloaded, critically overlapped surface coils were well decoupled to the level below −20 dB. However, when loaded with a human head, the best decoupling achieved between adjacent surface coils was approximately −11 dB, which corresponds to $R_{12}/R \sim 0.3$. According to Equation [4], the ratio of the RID-induced reactance to resistance (i.e. imaginary to real changes in the off-diagonal elements) is approximately equal to $2Q_0\xi$. For example, for $Q_0 \sim 200$ and $\xi \sim 0.07$ ($\Delta f \sim 20$ MHz), we obtained the value of ~30. As the induced reactance has to be equal to the mutual inductance between the surface coils, the RID-induced resistance is $\omega kL/2Q_0\xi$. For critically overlapped surface coils (~13.5 mm in our case), the mutual inductance (or k) is close to zero; therefore, the resistive component R_{12} remains, limiting decoupling to −11 dB. As the RID induces both reactive and resistive components, we induced a small inductive component by reducing the overlap by ~1.5 mm to 12 mm, generating k in the range from 0.02 to 0.025 (mutual inductance $M \sim 3$–4 nH). Using the RID shown in Fig. 6, we were then able to compensate (−24 dB coupling) for both the resistive and reactive (induced by changing overlap) components of Z_{12}, whilst minimizing B_1 distortion. For the nonadjacent ($\Delta n = 2$) surface coils, where resistive coupling is negligible, we used conventional non-RID. The Q_U value of individual surface coils was 270, in comparison with 360 for a single surface coil of the same size. Despite some reduction in Q_U, we obtained a Q_U/Q_L ratio of 2.7 or greater for all coils with the head, including the less loaded anterior surface coils.

Previously, we have demonstrated that multiple-channel, single-row (1×8) and double-row (2×8) 7-T transceiver phased arrays can be constructed successfully using conventional non-RID circuits, consisting of two small, strongly coupled loops, each connected in series with the adjacent surface coils (4,9). The decoupling was adjusted mechanically by changing the position of the loops with respect to each other. Mutual inductance is strongly dependent on surface coil loading determined by the coil to sample separation. As the decoupling is not adjusted on a patient-by-patient basis, it is crucial to maintain similar loading, e.g. by maintaining a similar distance from each coil to the sample. Appropriate loading must also be maintained to optimize the coil efficiency and the SNR. The substantial increase in the number of decoupling units for multi-row arrays [e.g. 40 in a 2×8 array (8–10)] makes even the one-time mechanical adjustment prior to deployment cumbersome for experimental use. Unlike nonresonant decoupling, where the physical separation and/or orientation between the inductive loops must be adjusted, the RID method provides an easy way to perform the initial adjustment of the decoupling by changing the resonance frequency of the circuit (i.e. adjustment of a single variable capacitor).

When using RID circuits, their geometry and placement are critical in minimizing the perturbation to the B_1 field generated by the individual coils in the array. All attempts to utilize previously described RID geometries (21–23) to decouple a pair of 7.5 cm × 9 cm surface coils failed. As shown in Fig. 5B, even a

Copyright © 2013 John Wiley & Sons, Ltd.

NMR IN BIOMEDICINE

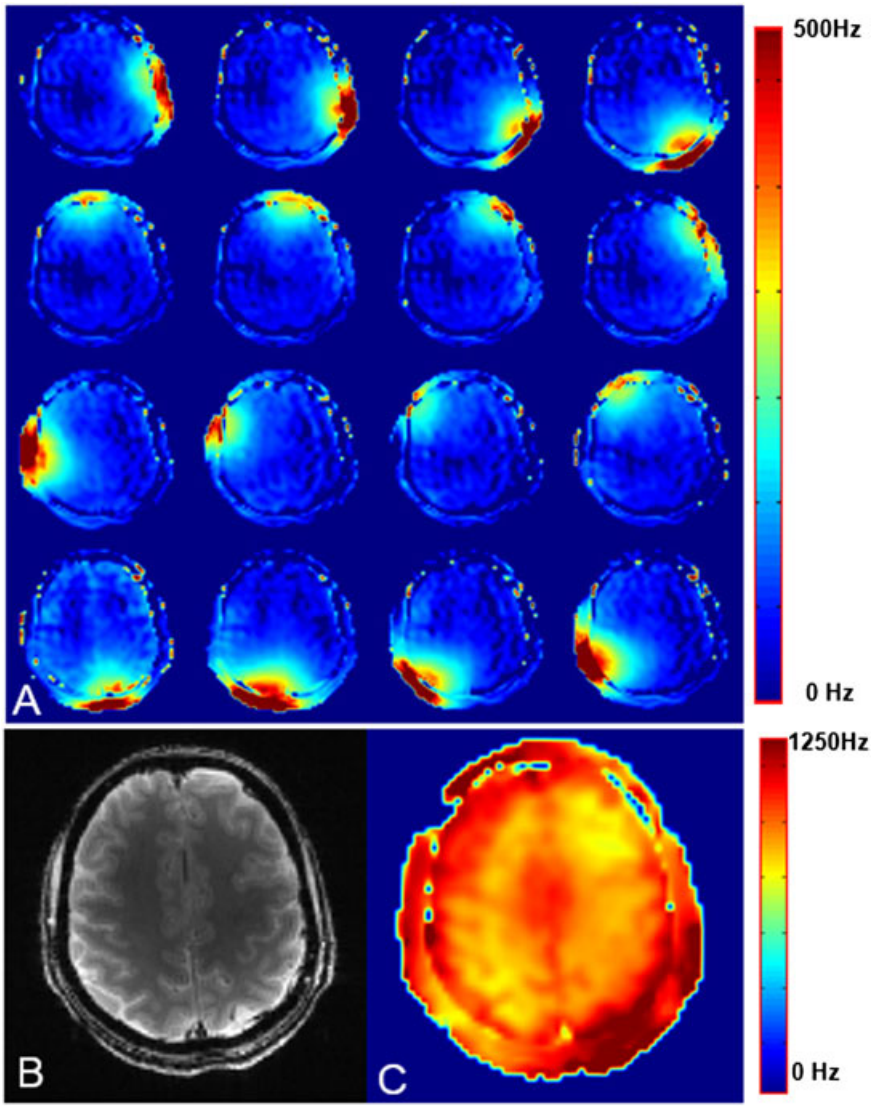

Figure 8. (A) Axial B_1^+ maps for individual surface coil elements. Axial image (B) and corresponding B_1^+ map (C) obtained using the 16-coil (1×16) overlapped array.

very small 16-mm 'flat' RID circuit (21) produces substantial distortions of the B_1 field of the array. Importantly, these distortions are seen at distances much greater than the size of the RID circuit itself. For 'flat' RID circuits, a substantial increase in Q_L (i.e. decrease in loading) in comparison with nonresonant decoupling is observed at distances of up to 7 cm separation between the object and the array (Fig. 7). When the difference between f_0 and f_L, Δf, becomes too small, even small resonant circuits can produce substantial distortion in the B_1 field of the array. To increase the Δf value, the coupling between the RID and surface coils, k_0, must be increased. Without substantially modifying the RID geometry, k_0 can only be increased by increasing the size of the RID loops. As larger RID loops extend the spatial extent of the distortion, all attempts to minimize it simply by changing the size of the RID circuit failed (Fig. 5). Thus, the geometry of the RID circuit plays an important role in enabling the size of the RID circuit to be kept small, whilst keeping k_0 sufficiently large. Using the optimized RID circuits shown in Fig. 6 we were able to simultaneously satisfy both of these requirements.

CONCLUSIONS

We have developed and experimentally verified a novel inductive decoupling method using a RID coil, which compensates for both the reactive and resistive components of the mutual impedance between the adjacent surface coils. After optimizing the geometry of the RID circuit, the method provides an easy way of adjusting the decoupling by changing the resonance frequency.

Acknowledgements

The National Institutes of Health provided grant support (grant numbers R01-EB009871, R01-EB011639 and R01NS081772).

REFERENCES

1. Adriany G, Van de Moortele P-F, Wiesinger F, Moeller S, Strupp JP, Andersen P, Snyder C, Zhang X, Chen W, Pruessmann KP, Boesiger P, Vaughan JT, Uğurbil K. Transmit and receive transmission line arrays for 7 Tesla parallel imaging. Magn. Reson. Med. 2005; 53: 434–445.

 Copyright © 2013 John Wiley & Sons, Ltd.

2. Mao W, Smith MB, Collins CM. Exploring the limits of RF shimming for high-field MRI of the human head. Magn. Reson. Med. 2006; 56(4): 918–922.
3. Ibrahim TS, Tang L. Insight into RF power requirements and B_1 field homogeneity for human MRI via rigorous FDTD approach. J. Magn. Reson. Imaging, 2007; 25(6): 1235–1247.
4. Avdievich NI, Pan JW, Baehring JM, Spencer DD, Hetherington HP. Short echo spectroscopic imaging of the human brain at 7 T using transceiver arrays. Magn. Reson. Med. 2009; 62: 17–25.
5. Kozlov M, Turner R. Analysis of RF transmit performance for a multi-row multi-channel MRI loop array at 300 and 400 MHz. *Proceedings of the Asia-Pacific Microwave Conference*, Melbourne, Australia, 2011; 1190–1193.
6. Katscher U, Börnert P, Leussler C, van den Brink JS. Transmit SENSE. Magn. Reson. Med. 2003; 49: 144–150.
7. Zhu Y. Parallel excitation with an array of transmit coils. Magn. Reson. Med. 2004; 51: 775–784.
8. Zhang Z, Yip CY, Grissom W, Noll DC, Boada FE, Stenger VA. Reduction of transmitter B1 inhomogeneity with transmit SENSE slice-select pulses. Magn. Reson. Med. 2007; 57(5): 842–847.
9. Avdievich NI. Transceiver phased arrays for human brain studies at 7 T. Appl. Magn. Reson. 2011; 41(2): 483–506.
10. Gilbert KM, Belliveau J-G, Curtis AT, Gati JS, Klassen LM, Menon RS. A conformal transceive array for 7 T neuroimaging. Magn. Reson. Med. 2012; 67: 1487–1496.
11. Shajan G, Hoffmann J, Scheffler K, Pohmann R. 16-Element dual-row transmit array for 3D RF shimming at 9.4 T. *Proceedings of the 20th Annual Meeting ISMRM*, Melbourne, Australia, 2012; 308.
12. Adriany G, Auerbach EJ, Snyder CJ, Gözübüyük A, Moeller S, Ritter J, Van de Moortele PF, Vaughan T, Uğurbil K. A 32-channel lattice transmission line array for parallel transmit and receive MRI at 7 Tesla. Magn. Reson. Med. 2010; 63(6): 1478–1485.
13. Wu B, Wang C, Kelley DAC, Xu D, Vigneron DB, Nelson SJ, Zhang X. Shielded microstrip array for 7 T human MR imaging. IEEE Trans. Med. Imaging 2010; 29: 179–184.
14. Tropp J. Mutual inductance in the bird-cage resonator. J. Magn. Reson. 1997; 126: 9–17.
15. Roemer PB, Edelstein WA, Hayes CE, Souza SP, Mueller OM. The NMR phased array. Magn. Reson. Med. 1990; 16: 192–225.
16. Kraff O, Bitz AK, Kruszona S, Orzada S, Schaefer LC, Theysohn JM, Maderwald S, Ladd ME, Quick HH. An eight-channel phased array RF coil for spine MR imaging at 7 T. Invest. Radiol. 2009; 44(11): 734–740.
17. Keil B, Alagappan V, Mareyam A, McNab JA, Fujimoto K, Tountcheva V, Triantafyllou C, Dilks DD, Kanwisher N, Lin W, Grant PE, Wald LL. Size-optimized 32-channel brain arrays for 3 T pediatric imaging. Magn. Reson. Med. 2011; 66: 1777–1787.
18. Wright SM. Full-wave analysis of planar radiofrequency coils and coil arrays with assumed current distribution. Conc. Magn. Reson. B: Magn. Reson. Eng. 2002; 15(1): 2–14.
19. von Morze C, Tropp J, Banerjee S, Xu D, Karpodinis K, Carvajal L, Hess CP, Mukherjee P, Majumdar S, Vigneron DB. An eight-channel, nonoverlapping phased array coil with capacitive decoupling for parallel MRI at 3 T. Conc. Magn. Reson. B: Magn. Reson. Eng. 2007; 31: 37–43.
20. Avdievich NI, Pan JW, Hetherington HP. Novel inductive decoupling for single- and double-tuned transceiver phased arrays to compensate for both reactive and resistive components of the mutual impedance. *Proceedings of the 20th Annual Meeting ISMRM*, Melbourne, Australia, 2012; 2806.
21. Aal-Braij R, Peter A, Del Tin L, Korvink JG. A novel inter-resonant coil decoupling technique for parallel imaging. *Proceedings of the 17th Annual Meeting ISMRM*, Honolulu, HI, USA, 2009; 2974.
22. Soutome Y, Otake Y, Bito Y. Vertical loop decoupling method for gapped phased-array coils. *Proceedings of the 19th Annual Meeting ISMRM*, Montreal, QC, Canada, 2011; 1859.
23. Li Y, Xie Z, Pang Y, Vigneron D, Zhang X. ICE decoupling technique for RF coil array designs. Med. Phys. 2011; 38(7): 4086–4093.
24. Harpen MD. Radiative losses of a birdcage resonator. Magn. Reson. Med. 1993; 29(5): 713–716.
25. Pan JW, Twieg DB, Hetherington HP. Quantitative spectroscopic imaging of the human brain. Magn. Reson. Med. 1998; 40: 363–369.
26. Beck BL, Jenkins KA, Rocca JR, Fitzsimmons JR. Tissue-equivalent phantoms for high frequencies. Conc. Magn. Reson. B: Magn. Reson. Eng. 2004; 20B(1): 30–33.
27. Picard L, Blackledge M, Decorps M. Improvements in electronic decoupling of transmitter and receiver coils. J. Magn. Reson. B 1995; 106: 110–115.
28. Sucher M, Fox J (eds). *Handbook of Microwave Measurements*. Willey & Sons, Polytechnic Press of the Polytechnic Institute of Brooklyn: New York, London; 1963.

Copyright © 2013 John Wiley & Sons, Ltd.